






## Microbial biosignature preservation in carbonated serpentinite from the Samail Ophiolite, Oman

Jon Lima-Zaloumis <sup>1</sup>✉, Anna Neubeck <sup>2</sup>, Magnus Ivarsson<sup>3</sup>, Maitrayee Bose<sup>1</sup>, Rebecca Greenberger<sup>4</sup>, Alexis S. Templeton <sup>5</sup>, Andrew D. Czaja<sup>6</sup>, Peter B. Kelemen <sup>7</sup> & Tomas Edvinsson <sup>8</sup>

Serpentinization is a geological process involving the interaction of water and ultramafic rock, the chemical byproducts of which can serve as an energy source for microbial communities. Although serpentinite systems are known to host active microbial life, it is unclear to what extent fossil evidence of these communities may be preserved over time. Here we report the detection of biosignatures preserved in a mineralized fracture within drill cores from the Samail Ophiolite in Oman. Two varieties of filamentous structures were identified in association with iron oxide precipitates. The first type are interpreted as likely microbial remains, while the second type are recognized as potentially microbiological dubiofossils. Additionally, laminated structures composed of carbon and nitrogen rich material were identified and interpreted as having a microbially-associated origin. Our observations affirm the potential to detect subsurface microbial communities within serpentinizing environments and highlight a unique taphonomic window to preserve evidence of rock-hosted life.

<sup>1</sup>Arizona State University, School of Earth and Space Exploration, PO Box 871404 Tempe 85287-1404 AZ, USA. <sup>2</sup>Uppsala University, Department of Palaeobiology Geocentrum, Villavägen 16, 752 36 Uppsala, Sweden. <sup>3</sup>Swedish Museum of Natural History, Department of Palaeobiology, P.O. Box 50007, SE-104 05 Stockholm, Sweden. <sup>4</sup>Caltech Division of Geological and Planetary Sciences, 1200 E. California Blvd., Pasadena 91125 CA, USA. <sup>5</sup>University of Colorado, Department of Geological Sciences, UCB 399, Boulder 80309 CO, USA. <sup>6</sup>University of Cincinnati, Department of Geology, 500 Geology-Physics, Cincinnati 45221-0013 OH, USA. <sup>7</sup>Columbia University Lamont-Doherty Earth Observatory, 211 Comer, 61 Route 9W - PO Box 1000, Palisades 10964 NY, USA. <sup>8</sup>Uppsala University, Department of Materials Science and Engineering, Ångströmlaboratoriet, Lagerhyddsvägen 1 Box 35, 751 03 Uppsala, Sweden. ✉email: [jzaloumi@asu.edu](mailto:jzaloumi@asu.edu)

Since their recognition as important geochemical sources of energy for life, serpentinites have become high-priority targets for directly investigating the existence and distribution of microbial life in the Earth's deep continental and oceanic subsurface<sup>1–4</sup>. Serpentinizing systems are also astrobiologically-relevant environments, where serpentine has been identified by remote sensing observations on Mars<sup>5–8</sup>, and is hypothesized to occur on other planetary environments, such as deep rock-water interfaces within Europa, Enceladus, and other bodies<sup>9–15</sup>. Serpentinizing systems may also have facilitated the origins of life<sup>9,16–24</sup>, further highlighting their significance as astrobiological targets.

In detail, water-rock reactions associated with serpentinization can generate direct sources of chemical energy and facilitate favorable geochemical conditions for microbial growth. In the presence of iron-bearing olivine and pyroxene phases, water is reduced during the oxidation of Fe<sup>2+</sup>, resulting in the precipitation of magnetite and ferric iron-bearing serpentine minerals, as well as the formation of molecular H<sub>2</sub><sup>25–27</sup>. This H<sub>2</sub> can be utilized as a metabolic fuel source by autotrophic microbial organisms such as methanogenic archaea and other hydrogen-oxidizing organisms<sup>28–31</sup>. Available H<sub>2</sub> may also react with inorganic carbon to form reduced carbon compounds<sup>32–34</sup>, which may be utilized as an energy and carbon source for methanotrophic archaea and other diverse heterotrophs<sup>31,35,36</sup>. Abiotic H<sub>2</sub>, CH<sub>4</sub> and organic acid generation associated with serpentinization therefore serves as an important energy source for microbial metabolisms, particularly in dark subsurface environments where photosynthesis is precluded<sup>2,31,37</sup>. Another key geobiological implication of serpentinization occurs as a consequence of the production of extremely reduced and hyperalkaline fluids that, when in contact with shallow aquifers at or near equilibrium with Earth's surface conditions, result in fluid mixing zones exhibiting sharp Eh and pH gradients that can facilitate a host of microbial metabolisms including sulfur, iron, and nitrogen cycling<sup>4,38–43</sup>.

In addition to supporting active microbial communities, fluid circulation during serpentinization may also create a unique taphonomic environment to capture and preserve fossil evidence of microbial life. Fracture-filling carbonate precipitation or complete whole rock carbonation is commonly observed among active and ancient serpentinized ultramafic deposits worldwide and is understood to occur as serpentinization proceeds in the presence of dissolved CO<sub>2</sub><sup>44–52</sup>. Carbonate precipitates are known to capture and preserve a variety of morphological and chemical biosignatures throughout Earth's history, and thus may represent important targets for the search for microbial remains beyond Earth<sup>53,54</sup>. In the present study, we explore whether subsurface fracture networks associated with serpentinization may serve as habitable niche environments, and more specifically whether evidence of microbial life may become preserved within associated fracture-filling carbonate precipitates. Here we report the detection of several structures resembling microbial biosignatures found within drill core samples of the largest subaerial exposure of mantle peridotite on Earth, the Samail Ophiolite in Oman.

## Results

**Sampling and vein description.** We first used optical petrology to analyze 60 samples spanning three drill cores from the active peridotite alteration zone of the Samail ophiolite in Oman acquired via the International Continental Scientific Drilling Program's (ICDP) Oman Drilling Project (Oman DP)<sup>55,56</sup>. Drill core locations along with their stratigraphic context within the ophiolite sequence are shown in Supplementary Fig. S1. To search for potential microbial biosignatures, we targeted core intervals

displaying prominent white mm to cm thick mineralized veins, which occurred most frequently in the upper 15 meters of core material below present surface<sup>57,58</sup>. Of the sections investigated, sample “BA1B 4-4 3-8” contained visible structures that resembled fossilized microbial remains. This specimen was sampled from hole BA1B (22.866N, 58.710E; Fig. S1) at a depth of 11.06 meters below surface and consists of a prominent ~9 mm thick carbonate filled fracture spanning across the sample approximately 35° relative to the coring direction (Fig. 1A).

Under plane-polarized light, the vein is characterized by coarse interlocking rhombic crystals with clear colorless interiors and grain boundaries. The primary vein mineralogy is composed of aragonite as determined by Raman spectroscopy (Fig. S2). Successive stages of carbonate precipitation resulting from crack-seal style vein fracturing can be seen by numerous linear cross-cutting fractures that are filled with later generations of carbonate growth and are further highlighted in areas where earlier carbonate crystal boundaries have been encrusted by orange and red colored iron oxide precipitates (Fig. 1). Along with iron oxides, there are adjacent opaque euhedral sulfides cemented throughout the vein, sometimes appearing intermixed with iron oxides (e.g., Fig. S3). Also cemented within the vein are brecciated fragments of an earlier waxy green serpentine vein (labeled “srp” in Fig. 1), many fragments of which are seen encrusted by rinds of iron oxide precipitates and cemented in place by sparry carbonate precipitates.

Within this vein, there is a small area containing structures resembling morphological biosignatures (Fig. 1A, red box). This zone represents a distinct stage of fracturing and precipitation as shown by near-total encrustation by iron oxide precipitates along its perimeter, which defines a roughly polygonal area approximately 1.3 mm by 0.5 mm in size (Fig. 1B, area outlined by red dashes). This iron oxide encrusted polygonal zone is bounded on one side by an earlier brecciated “waxy green” serpentine vein and on the remaining sides by apparently distinct generations of aragonite precipitates. Within the polygonal zone there are two varieties of filamentous structures as well as laminated precipitates resembling microstromatolites as described below.

**Filamentous structures.** Embedded within the iron-oxide encrusted polygonal zone, we recognize two distinct filamentous morphotypes referred to here as “Type A” and “Type B”. Type A filaments appear larger in thickness and length than Type B, with some specimens exhibiting a maximum length of 70 μm, although longer filaments may occur that are either obscured by pervasive iron oxide precipitates or have been truncated during thin section production. The diameter of Type A filaments ranges from 1.9 μm to 3.6 μm (mean = 2.7 μm; SD (1 σ) = 0.41 μm; n = 83; Fig. S4). Type A filaments occur either floating within the aragonite matrix where filaments are seen entwined among clots of flocculent iron oxide precipitates (Fig. 2B, G), or they appear anchored to the thick iron oxide encrusted walls of the polygonal zone and extend unidirectionally toward the interior of the polygonal zone (Figs. 2A, 3A). Type A filaments exhibit several distinguishing morphological characteristics including rounded terminal filament ends (Fig. 2A); a visible hollow central strand encircled by a marginal wall exhibiting uniform thickness (Fig. 2A, D, F); occasional budding features along the length of the filament (Fig. 2A black arrow); branching of filaments forming either T or Y junctions (e.g., Fig. 2B, F, G); and septal separations along filaments that do not occur at regular intervals (e.g., Fig. 2D). Additionally, some of these septal divisions appear to display narrow channel-like structures (Fig. 2E).

Type B filaments are smaller in size having an observed diameter of 0.6–1.3 μm (mean = 0.9 μm; SD (1 σ) = 0.17 μm;

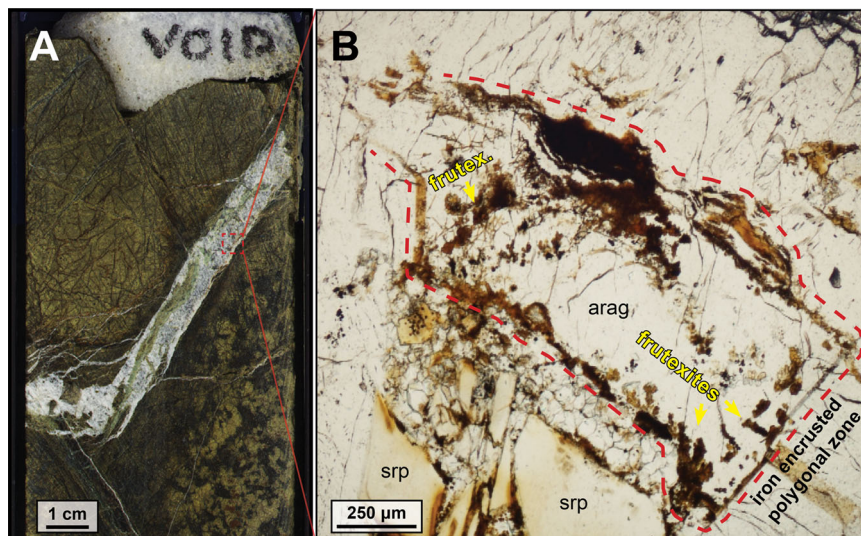


**Fig. 1** Context view of fossil-bearing carbonate vein. **A** split core view of vein from sample “BA1B 4-4 3-8”, sampled from 11.06 m depth. The red box shows the location of **B** (not to scale). **B** Petrographic view of the iron encrusted “polygonal zone” that contains fossilized microbial biosignatures. The matrix is composed of aragonite (labeled “arag”), and a brecciated waxy green serpentine (labeled “srp”) clast bounds the bottom margin of the polygonal zone. The locations of *Frutexites*-like microstromatolite structures are indicated by arrows.

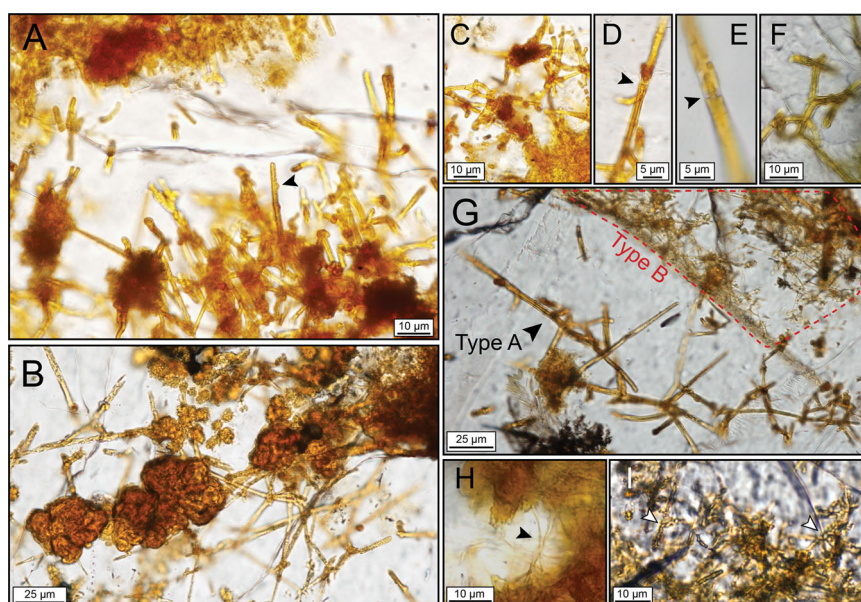


**Fig. 2** Filamentous structures preserved within the serpentine-hosted aragonite vein shown via transmitted light microscopy. **A** Type A filaments anchored to the iron-encrusted polygonal zone wall. Filaments here display rounded terminal ends and occasional budding along stalks (black arrow). **B** Type A filaments among clusters of laminated and flocculent iron oxide precipitates. **C** Type A filament interspersed among iron oxides. **D** Type A filament showing branching at septate division. **E** Type A filament displaying narrow channel-like structure along septal division. **F** Example of potential anastomosing among Type A filaments. **G** Branching Type A filaments adjacent to a cluster of Type B filaments (outlined in red), indicating relative size difference between the two morphotypes. **H** Thin Type B filaments spanning across iron oxide precipitates. **I** Dense cluster of Type B filaments with some specimens resembling twisted stalks (white arrows).

$n = 45$ ; Fig. 2H, I, and S4). The maximum length of Type B filaments observed was 11.2  $\mu\text{m}$ , although most filament terminations are visibly obscured by surrounding iron oxides or are cut off by the limited thin sectioned volume. Type B filaments do not appear to have septate partitions, instead occurring as continuous filaments. Like the Type A filaments, most Type B filaments were observed as tightly intertwined bundles among clusters of iron oxide precipitates floating within the carbonate matrix and along the iron-encrusted polygonal zone walls (Fig. 2H and I).

Energy-Dispersive X-ray Spectroscopy (EDS) mapping of these iron oxide and filament clusters shows an elemental composition dominated by iron and carbon (Fig. 3A EDS inset). Notably, the elevated carbon concentrations are inversely correlated with the presence of calcium, indicating that the carbon signal is not due to the surrounding  $\text{CaCO}_3$  aragonite vein matrix (Fig. 3A). Attempted Raman measurements of filament and iron oxide clusters resulted in intense fluorescence. However, Nanoscale Secondary-Ion Mass Spectroscopy (NanoSIMS) chemical maps

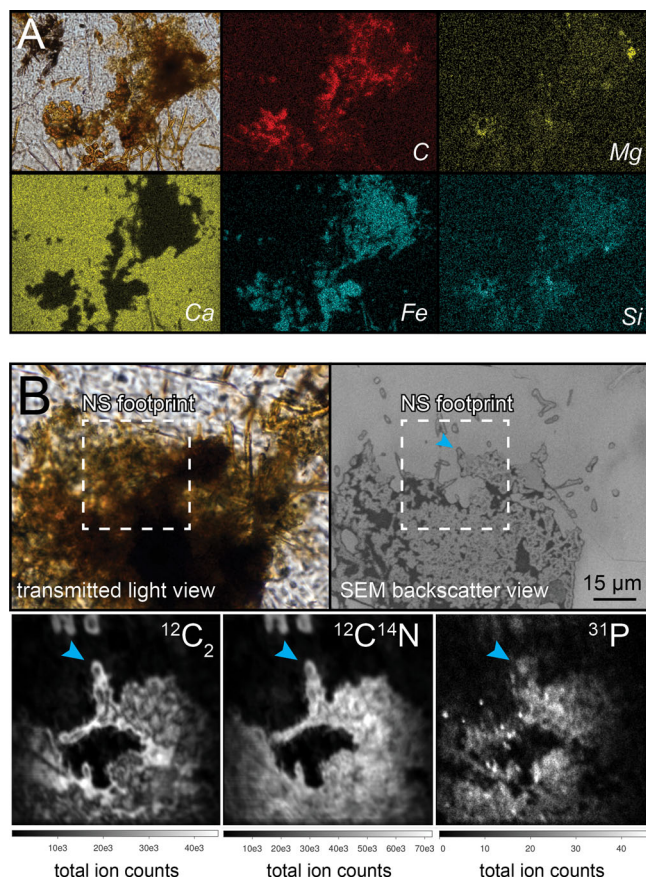


**Fig. 3 Compositional maps of iron oxide & filament clusters.**

**A** Transmitted light image and accompanying EDS maps of iron oxide precipitates containing numerous entwined filamentous structures. EDS data show enrichment of C correlated to Fe. The C enrichment is inversely correlated with Ca, indicating that the enriched C signal does not appear to be due to aragonite. **B**, upper) View of NanoSIMS (NS) mapping area (white dashes) imaged in transmitted light (left) and SEM backscatter detection (right). Note that the SEM view shows the extent of surface-exposed iron oxides and filaments (indicated by blue arrow) measured by NanoSIMS. In transmitted light, the filaments are difficult to distinguish due to the dense accumulation of iron oxides. **B**, lower) NanoSIMS ion maps of carbon, nitrogen, and phosphorous associated with iron oxide and filament cluster. The blue arrow points to Type A filaments that have been further revealed by the sputtering process. The field of view for each ion map is  $40\ \mu\text{m} \times 40\ \mu\text{m}$ , and brighter features correspond to higher total ion counts per pixel as shown by the lower scalebar.

corroborated the presence of C and additionally showed the presence of nitrogen, measured as the  $^{12}\text{C}^{14}\text{N}$  ion, and phosphorus (Fig. 3B). The NanoSIMS mapping area includes visible Type A filaments and shows that they are associated with carbon and nitrogen (Fig. 3B, blue arrow).

**Laminated iron oxides resembling *Frutexites*.** In addition to the filamentous structures described above, there are accumulations of iron oxide precipitates that form laminated structures resembling microdigitate stromatolites. These structures are found throughout the interior of the polygonal zone and anchored along the iron-encrusted boundary (Fig. 1A yellow arrows and Fig. 4) and display a growth orientation towards the center of the polygonal zone. The structures exhibit a characteristic digitate branching pattern (Fig. 4A, B) and are similar morphologically and compositionally to stromatolitic structures termed *Frutexites*<sup>59–61</sup>, which have been described in a number of

subsurface environments<sup>62–64</sup> and are generally restricted to settings with low light availability and low rates of sedimentation<sup>63,65</sup>. Scanning Electron Microscopy (SEM) shows that these *Frutexites*-like structures are composed of alternating laminae that generally thicken towards the apex of the stromatolite growth direction (Fig. 4C). EDS analyses show that electron-dark laminae are dominated by C with lower relative concentrations of O, Fe, Ca, and Si (Fig. 4C spots 1 & 3), while electron-bright laminae are dominated by O, Fe, C, Ca, and lower relative concentrations of Si and Mg (Fig. 4C spot 2). Raman analysis of the electron-dark laminae yield vibrational bands at  $\sim 1350\ \text{cm}^{-1}$  and  $\sim 1600\ \text{cm}^{-1}$ , corresponding to disordered “D” and graphitic “G” bands characteristic of macromolecular carbonaceous material<sup>66,67</sup> (Fig. 4). NanoSIMS ion maps of these laminated *Frutexites*-like structures corroborates the presence of C and additionally show the presence of nitrogen, measured as the  $^{12}\text{C}^{14}\text{N}$  ion (Fig. 4D), which forms as clearly distinguishable laminae visible in the NanoSIMS ion maps.

**Iron oxide distribution and potential sources.** As shown above, these filamentous and stromatolitic structures appear closely associated with iron oxide precipitates. Visible-shortwave infrared (VSWIR) hyperspectral mapping conducted during the core logging phase of Oman DP highlights the distribution of  $\text{Fe}^{2+}$  and  $\text{Fe}^{3+}$  throughout the vein and surrounding drill core interval (Fig. S5). The iron oxides associated with the preserved filaments and *Frutexites*-like structures display a 685 nm wavelength absorption feature, which represents the electronic transition of  $\text{Fe}^{3+}$  and is characteristic of iron oxides such as goethite, hematite, and ferrihydrite<sup>68,69</sup>. Notably, this absorption feature occurs only in a few small zones throughout the carbonate vein (Fig. S5c). The heterogeneous distribution of this mineral within the vein, which forms as encrustations surrounding the once-open fracture space (e.g., Fig. 1), indicates that conditions favorable for its precipitation occurred only during a few specific intervals of crack-seal vein formation.

There are several potential sources of  $\text{Fe}^{2+}$  for oxidation to have occurred within the vein. A 750 nm absorption feature corresponding to an  $\text{Fe}^{2+}/\text{Fe}^{3+}$  intervalence charge transfer was mapped, which indicates the presence of mixed  $\text{Fe}^{2+}$  and  $\text{Fe}^{3+}$  found in serpentine<sup>70,71</sup>. This feature is most strongly observed within the neighboring brecciated “waxy green” serpentine vein that bounds one side of the iron-encrusted polygonal zone (visible in Fig. 1A). This absorption feature indicates a potential local source of  $\text{Fe}^{2+}$ , although ferrous iron may have also been sourced from reducing fluids outside of the immediate vicinity of the fracture. Geochemical analysis of fluids collected from nearby boreholes does show that  $\text{Fe}^{2+}_{(\text{aq})}$  is present at 9 to 36 micromolar concentration<sup>2</sup>, and synchrotron-based x-ray fluorescence mapping of late-stage waxy green serpentine veins in BA1B also shows that the Fe-speciation is dominated by Fe(II)<sup>72</sup>.

## Discussion

**Biogenicity of filamentous structures.** As shown herein, fracture-filling carbonate veins in serpentinizing systems can preserve structures resembling microbial biosignatures in the form of filamentous and stromatolitic morphotypes. As with any assessment of biogenicity, multiple lines of evidence must be considered to determine whether such structures represent actual remnants of past life<sup>73–75</sup>. Structures resembling filamentous microfossils can be challenging to interpret due to their often-simple morphology and may instead be attributed to abiogenic processes<sup>76</sup>. Several previous reports have described laboratory-grown abiotic “biomorph” structures with characteristics consistent with microbial cells<sup>77–81</sup>, and furthermore Garcia-Ruiz

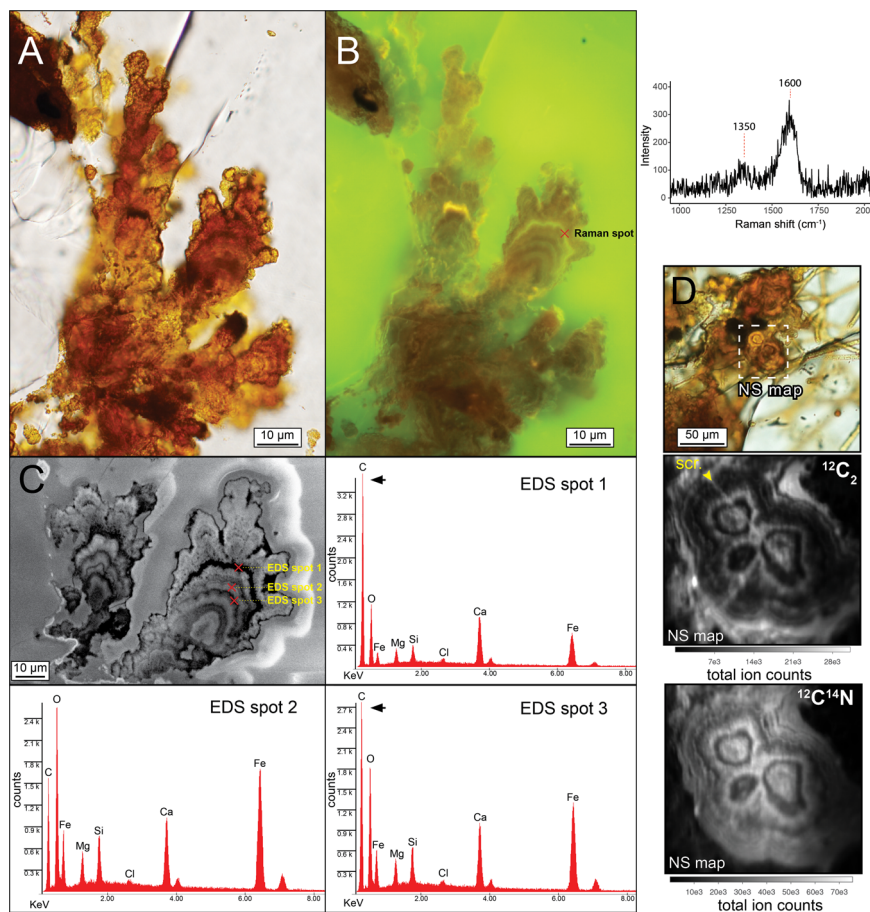


**Fig. 4** *Frutexitis*-like microstromatolitic structures and associated compositional maps. **A** Branching columnar structures display feint lamination under plane-polarized light. **B** Fluorescence microscopy reveals fine laminations in greater detail. Raman spectroscopic analysis of laminae show the presence of “D” and “G” vibrational bands at  $-1350\text{ cm}^{-1}$  and  $-1600\text{ cm}^{-1}$  respectively (shown at right), indicative of macromolecular carbonaceous material. **C** SEM secondary electron image shows microscale laminations and marks the locations of EDS spot analyses. EDS measurements show alternation between dark C-rich laminae (e.g., spot 1 & 3), and bright laminae dominantly composed of O, C, Ca, Fe, Si, and Mg (e.g., spot 2). **D** location of NanoSIMS mapping conducted on microstromatolites cut orthogonal to the growth direction by thin sectioning. Bottom panels of (**D**) show laminae containing nitrogen and carbon. A yellow arrow marks a surface scratch that appears in the  $^{12}\text{C}_2$  ion map introduced during sample preparation. Brighter features in both NanoSIMS images correspond to higher total ion counts per pixel.

et al. (2017)<sup>82</sup> have synthesized silica biomorph structures from alkaline spring waters derived from serpentinization. These studies highlight the many challenges in determining the origin of similar structures preserved in the rock record. More recently, McMahon et al. (2021)<sup>83</sup> described filamentous and microstromatolitic “dubiofossils” of uncertain origin occurring within Jurassic serpentine-hosted carbonate veins. These authors argue that such structures could have formed among geochemical conditions similar to “chemical gardens” that are known to precipitate abiotic filamentous forms<sup>83</sup>. Given these challenges, we argue that for some of the structures presented here there are several pieces of evidence that, when combined, enables a determination of their origin.

In support of a biological interpretation, the “Type A” filamentous specimens reported here display the following morphological characteristics: a uniform filament thickness along individual stalks, a normal size frequency distribution between specimens (Fig. S4), rounded terminal ends of filaments (Fig. 2A), and true septal separations (e.g., Fig. 2D). As noted by Rouillard et al. (2018)<sup>84</sup>, abiotic biomorphs grown in laboratory experiments typically exhibit a diverse and continuous range of morphology and size; in contrast, the morphotypes reported here are generally restricted to two primary types (i.e., “Type A”

and “Type B”) and display a consistent size distribution (Fig. S4). Many Type A filaments also display preferential anchoring onto the iron-oxide encrusted polygonal zone wall forming a dense cluster of filaments that exhibit a unidirectional growth orientation (Fig. 1B, Fig. 3A). Such non-random distribution and orientation may indicate behavioral activity<sup>85</sup>, although McMahon (2019) reported abiotic filamentous biomorphs grown in a sodium silicate solution initially tended toward a vertical growth orientation in laboratory experiments.

The overall morphology exhibited in Type A filaments appears relatively complex and is potentially consistent with a fungal origin as shown by several additional morphological features. These include the presence of branching along septal divisions (Fig. 1A–D, G), occasional budding along filament stalks (Fig. 1A black arrow), and the occurrence of narrow channel-like structures along some septal separations (e.g., Fig. 2E). Similar channel-like structures are common along septa in basidiomycete fungi and are referred to as “dolipore” structures<sup>86</sup>. Such features were admittedly rare however and may instead represent altered and degraded zones within the filament that coincidentally form symmetric channel-like spaces. Another defining characteristic of fungi is anastomoses, or connective branching between fungal filament stalks. We identified several potential anastomosing

filaments (e.g., Fig. 2D), however it was difficult to identify anastomoses unambiguously due to the dense accumulations of iron oxide precipitates that typically obscured observation. Given their potential similarity to known fungal morphotypes, we stress that features like branching and budding have also been shown to be replicated by abiotic “biomorph” structures produced in laboratory experiments<sup>80</sup>. Overall, we exercise caution in placing a definitive fungal interpretation for Type A filament specimens in favor of a more general claim that these structures are likely biological in origin.

Further evidence of filament biogenicity is indicated by their elemental composition. Here we show that Type A filaments are composed of carbon and nitrogen bearing material (Fig. 3), consistent with the presence of biologically derived organic material. Carbonaceous material (e.g., kerogen) associated with biomorphic structures has often been regarded as an indicator of biogenicity<sup>73,87</sup>, although abiotic pathways have been suggested to explain the occurrence of some carbonaceous microfossil-like structures<sup>77</sup>. Nitrogen associated with the microfossils described here provides further evidence of biogenicity as nitrogen is a key element present in a number of essential biomolecules and is known to occur among preserved biologically-derived carbonaceous material<sup>88–90</sup>. Overall, we argue that the coincidence of complex morphology, normal size distribution between specimens, and the presence of C and N bearing material together constitute robust evidence in favor of a biological interpretation.

Type B filaments may have a different source. These filaments exhibit a generally uniform thickness along their length and display normally distributed filament diameter sizes between specimens (Fig. S5). Occasionally, a helical stalk morphology was observed (e.g., Fig. 2I, black arrows), although this observation is potentially problematic due to their very small size and the limits of optical magnification. Although helical stalk morphologies are known to occur among iron oxidizing bacteria such as *Gallionella ferruginea*<sup>91</sup>, it should be noted that such morphologies have also been described in abiotic laboratory-grown biomorphs<sup>78,84</sup>. In terms of composition, we could not resolve individual Type B filaments within our generated chemical maps, thus their individual composition at present remains unknown. Given these factors, we cannot determine whether these specimens might represent abiotic “biomorphs” similar to those described by Cosmidis and Templeton (2016)<sup>78</sup>, Ruiz-Garcia et al. (2017)<sup>82</sup>, and McMahon et al. (2019)<sup>80</sup> among others. Further micro-analytical work involving precise extraction and analysis (e.g., synchrotron-based analytical methods) may yield additional information relevant to determining their origin. Indeed, it would not be surprising if conditions occur that enable the growth of both biological and abiotic “biomorph” structures together, particularly in fracture spaces exhibiting pronounced geochemical disequilibrium<sup>83</sup>. Further observational and experimental work regarding such structures is warranted to better understand their occurrence, particularly among geochemical conditions matching serpentinizing systems.

**Biogenicity of *Frutexites*-like microstromatolites.** Since their earliest descriptions<sup>59–61,92,93</sup>, *Frutexites* have traditionally been interpreted as organosedimentary structures formed by the influence of microbial activity. Given their prevalence in aphotic environments such as in deep marine sediments and within subsurface fissures and cavities, some authors have attributed *Frutexites* growth to cryptoendolithic/chemotrophic microbial activity<sup>94,95</sup>. Recently, modern *Frutexites* were investigated by Heim et al. (2017)<sup>64</sup> growing in the subsurface Äspö Hard Rock Laboratory in Sweden. Here, *Frutexites* structures were found coated in microbial exopolymer sheath material (EPS) containing

aggregates of coccoid, rod-shaped, and filamentous prokaryotic organisms. 454 pyrosequencing of the biofilm community showed a predominance of nitrogen and iron cycling communities including ammonia-oxidizing bacteria *Nitrosomonas*, nitrite oxidizing bacteria *Candidatus Nitroga*, *Nitrospira*, and *Nitrospina*, as well as iron oxidizing bacteria *Mariprofundus sp.* and *Gallionella ferruginia*. *Frutexites* were interpreted to form by active and passive biological processes including direct microbial oxidation of Fe(II) by iron oxidizing bacteria, indirect oxidation of Fe(II) via nitrite produced by the bacterial respiration of nitrate, and by iron oxide templating onto reactive organic surfaces such as cell walls and EPS material.

The laminated microstromatolitic structures we describe in this report are similar in composition and morphology to the *Frutexites* structures described above. As previously noted, the structures are composed of alternating laminae of iron oxide material (also containing Ca, C, Si, and Mg) and C+N rich material. Additionally, Raman analyses of the C + N rich laminae show vibrational bands consistent with the presence of macromolecular carbonaceous material. Although individual prokaryotic structures such as rods and coccoids were not observed within these very fine laminae, the presence of carbonaceous nitrogen-bearing material suggests a biological influence on their formation. We note that a scenario may have occurred where dissolved organics present among the fracture fluids adsorbed onto the *Frutexites*-like structures as well as the filaments and surrounding flocculent iron oxides before becoming entombed by carbonate. Although possible, we favor an interpretation where the organics were largely formed in situ due to contributions by filament biomass and possibly biofilm-derived EPS similar to that reported by Heim et al. (2017)<sup>64</sup>. In support of this, we argue that if the organics were only derived from ambient fluids, then we would not expect to see C + N rich material forming as distinct alternating laminations only among *Frutexites*, but rather carbonaceous material would be distributed similarly throughout all of the structures found in the polygonal zone.

**Habitability and preservation potential of serpentine-hosted fractures.** Another important criterion to consider when assessing biogenicity is the plausibility of the environment to host life, which is determined by assessing the broader geologic context of the specimen in question<sup>74,75</sup>. As previously noted, serpentinization processes can lead to the production of reduced compounds such as H<sub>2</sub>, CH<sub>4</sub> and NH<sub>4</sub>. Conditions favorable for microbial habitability can then be generated where these electron donors are microbially oxidized using electron acceptors such as sulfate, nitrate, and nitrite within mixing zones between extremely reducing hyperalkaline fluids and more oxidizing shallow aquifer fluids<sup>2</sup>. Leong and Shock (2020) reported generalized reaction pathways for low temperature serpentinizing systems and highlighted the production of hyperalkaline (pH > 11) fluids rich in Ca, OH, and H<sub>2</sub> and poor in Mg, Si and dissolved inorganic carbon (DIC). The mixing of such deep serpentinizing fluids with oxidized shallow aquifer fluids containing atmospherically-derived DIC results in the generation of steep geochemical gradients creating “hotspots” of thermodynamic disequilibria where microbial life may thrive<sup>39,42,96</sup>.

Leong et al. (2021)<sup>97</sup> reported fluid compositions at discharging spring sites at the Samail Ophiolite and determined that most of the sampled fluids are characterized by mixing between deep hyperalkaline Ca-OH rich/DIC-poor fluids with shallow Si-Mg rich/DIC-rich fluids. Strong Eh and pH gradients occur among the fluids here today as a result of ongoing serpentinization with values ranging from pH 8.5 to 11.2 and Eh +200 to -750 mV as measured by borehole fluid measurements taken nearby

the sampled cores<sup>4,57</sup>. Such geochemical gradients can facilitate microbial activity, and indeed an active albeit heterogeneously-distributed microbial ecosystem has been shown to occur here among sampled fluids<sup>2,43,98,99</sup> and among serpentinite core material with an average cell abundance of  $10^6$  cells/gram rock<sup>4</sup>.

Fortunately for the prospect of biosignature preservation, the mixing interval between deep serpentinizing fluids and shallow aquifers is associated with pervasive calcium carbonate precipitation that can serve to entomb in situ microbial communities. Hyperalkaline serpentinizing fluids that encounter aquifers containing atmospherically derived DIC results in carbonate saturation conditions and subsequent precipitation<sup>58</sup>. Furthermore, hydration and carbonation reactions associated with serpentinization result in an increase of the solid rock volume causing pressurization conditions that can lead to fracturing of the host rock<sup>48,100,101</sup>. Fractures created by this process, in addition to those created by local and regional tectonic processes, can function as conduits for water transport and may drive further serpentinization of newly exposed ultramafic material, though the details of such reaction-driven processes are still under active investigation<sup>102–106</sup>.

As we suggest here, these evolving fracture networks may become inhabited by microbial communities and subsequently sealed by carbonate minerals. It is important to note that of the 60 samples and associated thin sections investigated across three drill cores, we found discernable filamentous body fossils only within sample “BA1B 4-4 3-8”. In other words, not all carbonate mineralized fractures within the serpentinite environment appear to have been obviously inhabited by these filamentous morphotypes and subsequently fossilized. Given the apparently patchy distribution of these potential biosignatures, we suggest that fracture colonization might proceed during discrete intervals and locations depending on several factors including transient fluid redox conditions and vein accessibility. As previously noted, the heterogeneous distribution of iron oxide and sulfide phases within the “BA1B 4-4 3-8” vein matrix (Fig. S5) indicates that the fluid chemistry may have varied over the duration of ongoing crack-seal style fracture formation. Because preserved microbial biosignatures appear to be limited to the relatively small iron oxide bound polygonal zone within the vein (Fig. 1B), microbial colonization may have proceeded during a transitory period when sufficient concentrations of electron donors and acceptors were available, in this case when ferrous iron was available and fluid conditions favored iron oxidation and precipitation.

Additionally, the fracture space must also be accessible to organisms as they disperse throughout the fracture network. Fractures that form and remain unconnected to the larger inhabited fracture network might remain uninhabited regardless of whether they exhibit favorable redox conditions for microbial metabolisms. As reported by Templeton et al. (2021)<sup>4</sup>, the distribution of active microbial communities along the BA1B drill core appear highly heterogeneous with values ranging from  $10^7$  cells at the top of BA1B to  $10^1$  cells in the interior of some cores. Additionally, these authors report a several orders of magnitude difference in cell densities between samples with abundant veins than for samples of only core interiors. These authors suggest that fractures in this system may host microcolonies and/or dense biofilms, which may explain the observed heterogeneity. Consistent with these insights and the observations we present here, a conceptual model of fracture formation, microbial colonization, and eventual entombment is shown in Fig. 5.

Although it is difficult to estimate a specific time interval for when the fossils described here were initially entombed, it is clear from observed cross-cutting relationships with numerous other vein types occurring along the BA1B core, including black and white serpentinite veins, that carbonate veins and “waxy green”

serpentine veins are approximately coeval and represent the most recent vein type as shown by cross-cutting relationships<sup>57,107</sup>. Radiocarbon  $^{14}\text{C}$  dating measurements throughout the BA1B drill core indicate that 2/3rds of 30 sampled carbonate veins contain measurable  $^{14}\text{C}$ , corresponding to ages of 20 to 50 kyr, or 0.2% to 8% modern carbon in acid washed mineral separates<sup>57</sup>. However, additional difficulty arises from fact that fracturing and precipitation clearly occurs over multiple stages, thus a single vein likely has precipitates formed over a range of ages. Given this complexity, we do not know precisely when the “iron oxide polygonal zone” was open and subsequently sealed by precipitates. Regardless of the precise timing of fossilization of the specimens reported here, however, we emphasize the overall taphonomic potential for biosignature preservation in these systems as a result of pervasive carbonate precipitation.

As we proceed in our exploration for a microbial fossil record beyond Earth, it is important to identify and elucidate various taphonomic modes of microbial preservation that may plausibly occur in planetary environments. Given the possible ubiquity of ultramafic rock and water interactions throughout the solar system and beyond, we might expect serpentinization and associated carbonate precipitation to be common processes<sup>13</sup>. Here we show that such environments can lead to the preservation of morphological structures and associated chemical signatures that resemble microbial biosignatures. We advocate that serpentinite and carbonate assemblages should thus be considered potentially favorable targets for the exploration of fossil microbial communities beyond Earth. We also advocate for additional research to search for older examples of potential biosignatures in these systems and to understand the varieties of biosignatures that may become preserved. Recent work along these lines include dubiofossils reported by McMahon et al. (2021)<sup>83</sup>, preserved lipids and biomorphic structures reported by Klein et al. (2015)<sup>108</sup>, and lipid biomarkers reported by Zwicker et al. (2018)<sup>109</sup> and Newman et al. (2020)<sup>110</sup>. It should also be recognized that biosignature preservation may not be limited to carbonate precipitates in these environments. For example, Menez et al. (2012)<sup>111</sup> reported preserved organic material, interpreted as microbial remains, associated with hydrogarnet minerals within fully serpentinized seafloor peridotites. Such studies are warranted to better establish the extent of microbial preservation within these systems and ultimately to generate useful search strategies to find evidence of fossilized life within similar rocks beyond Earth.

### Methods summary

Drill core samples from the ICDP Oman Drilling Project were subsampled into 5 cm quarter core samples and serial thin sections were produced for each quarter core either with standard 40  $\mu\text{m}$  thickness or 200  $\mu\text{m}$  thickness. Optical and fluorescence microscopy was performed using Nikon SMZ1500 stereomicroscope, Nikon Eclipse E600 polarized petrographic microscope, and Olympus BX51 fluorescence microscope equipped with an Olympus DP71 detachable camera and an X-Cite series 120 external fluorescent light source. Scanning Electron Microscopy & Energy Dispersive X-Ray Spectroscopy analyses were conducted using a Zeiss Supra 35VP field emission electron microscope equipped with an Ametek EDAX Apollo X detector. EDX measurements were acquired using Ametek EDAX Genesis (V6.50) software. Samples were analyzed via Raman spectroscopy at the Uppsala University Angstrom Laboratory using a commercial Renishaw Invia Qontor Raman spectrometer with 355 nm UV incident laser, and at the University of Cincinnati using a Horiba T64000 Raman microscope using visible 514 nm laser line. Isotopic maps were acquired on an Ametek Cameca 50L NanoSIMS instrument at Arizona State University. Sample chips were cut

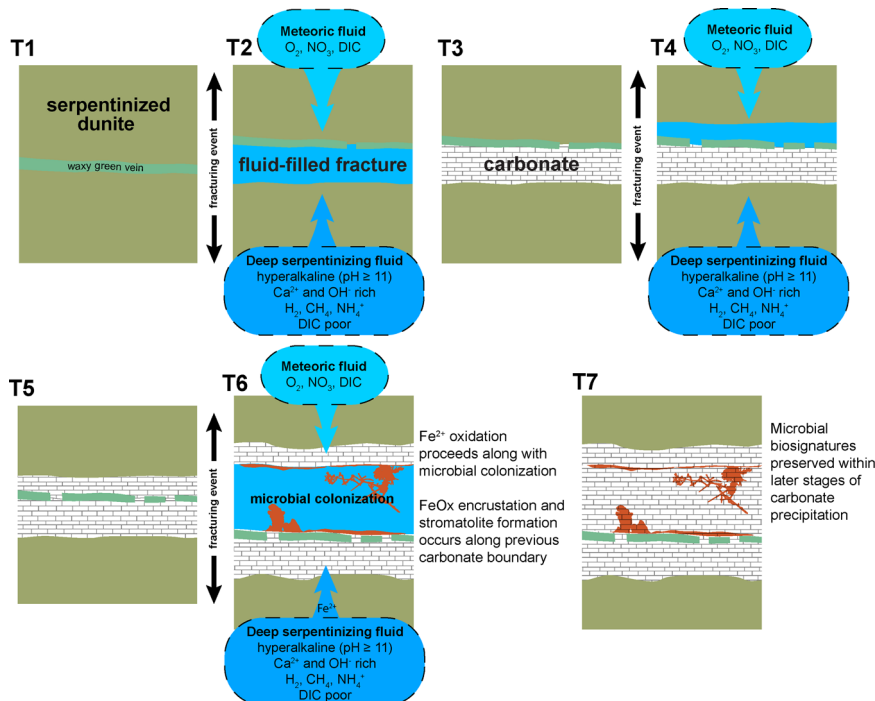


**Fig. 5 Conceptual model of biosignature preservation in serpentine-hosted carbonate veins.** Time 1 (T1) begins with serpentinized ultramafic host rock, followed by a brittle fracturing event (T2) resulting in fluid flow via adjoining connective fractures (represented by blue arrows above and below). Where deep hyperalkaline & reduced serpentinizing fluids rich in Ca and poor in DIC contact shallow meteoric fluids containing DIC, carbonate precipitation occurs resulting in sealing of the fracture (T3). Crack-and-seal style fracturing continues (T4–T6), with remnant material (e.g., preexisting “waxy green” serpentine vein) entombed within the carbonate. At T6, iron oxidation proceeds along with microbial colonization within the fracture space. When carbonate saturation is reached within the fracture space, another stage of precipitation occurs (T7) resulting in fossilization of the in situ microbial community.

from the thin section, cleaned, and embedded in indium-filled ring mount and subsequently gold-coated. The analysis was conducted by presputtering the mapping area (typically 40 μm x 40 μm) with a Cs<sup>+</sup> primary ion beam ~100 pA current. After presputtering, a smaller area was mapped within the presputtered region using a 1–3 pA beam current with a dwell time of 5msec/pixel, 256<sup>2</sup> pixels, and up to 40 frames.

**Reporting summary.** Further information on research design is available in the Nature Research Reporting Summary linked to this article.

### Data availability

All microscopic images as well as EDS and NanoSIMS chemical data presented here are available through an online repository using the following link: <https://doi.org/10.6084/m9.figshare.20549253.v1>.

Received: 25 May 2022; Accepted: 5 September 2022;

Published online: 07 October 2022

### References

- Schrenk, M. O., Brazelton, W. J. & Lang, S. Q. Serpentinization, carbon, and deep life. *Rev. Mineral. Geochem.* **75**, 575–606 (2013).
- Rempfert, K. R. et al. Geological and geochemical controls on subsurface microbial life in the Samail Ophiolite, Oman. *Front. Microbiol.* **8**, 56 (2017).
- Ivarsson, M., Bach, W., Broman, C., Neubeck, A. & Bengtson, S. Fossilized Life in Subseafloor Ultramafic Rocks. *Geomicrobiol. J.* <https://doi.org/10.1080/01490451.2017.1370517> (2018).
- Templeton, A. S. et al. Accessing the subsurface biosphere within rocks undergoing active low-temperature serpentinization in the Samail ophiolite (Oman Drilling Project). <https://doi.org/10.1002/ESSOAR.10506393.1> (2021).
- Schulte, M., Blake, D., Hoehler, T. & McCollom, T. Serpentinization and its implications for life on the early Earth and Mars. *Astrobiology* **6**, 364–376 (2006).
- Ehlmann, B. L., Mustard, J. F. & Murchie, S. L. Geologic setting of serpentine deposits on Mars. *Geophys. Res. Lett.* **37**, L06201 (2010).
- Oehler, D. Z. & Etiope, G. Methane seepage on mars: where to look and why. *Astrobiology* 1233–1264 <https://doi.org/10.1089/ast.2017.1657> (2017).
- Amador, E. S., Bandfield, J. L. & Thomas, N. H. A search for minerals associated with serpentinization across Mars using CRISM spectral data. *Icarus* **311**, 113–134 (2018).
- Sleep, N. H., Meibom, A., Fridriksson, T., Coleman, R. G. & Bird, D. K. H<sub>2</sub>-rich fluids from serpentinization: Geochemical and biotic implications. *Proc. Natl. Acad. Sci.* **101**, 12818–12823 (2004).
- Guo, W. & Eiler, J. M. Temperatures of aqueous alteration and evidence for methane generation on the parent bodies of the CM chondrites. *Geochim. Cosmochim. Acta.* **71**, 5565–5575 (2007).
- Sohl, F. et al. Subsurface water oceans on icy satellites: Chemical composition and exchange processes. *Space Sci. Rev.* **153**, 485–510 (2010).
- Glein, C. R., Baross, J. A. & Waite, J. H. The pH of Enceladus’ ocean. *Geochim. Cosmochim. Acta.* **162**, 202–219 (2015).
- Holm, N. G., Oze, C., Mousis, O., Waite, J. H. & Guilbert-Lepoutre, A. Serpentinization and the Formation of H<sub>2</sub> and CH<sub>4</sub> on Celestial Bodies (Planets, Moons, Comets). *Astrobiology* **15**, 587–600 (2015).
- Taubner, R. S. et al. Biological methane production under putative Enceladus-like conditions. *Nat. Commun.* **9**, 1–11 (2018).
- Vance, S. D. & Melwani Daswani, M. Serpentinite and the search for life beyond Earth. *Philos. Trans. A. Math. Phys. Eng. Sci.* **378**, 20180421 (2020).
- Shock, E. L. Hydrothermal systems as environments for the emergence of life. in *CIBA Foundation Symposia* (eds. Bock, G. R. & Goode, J. A.) 40–60 (Wiley, 1996). <https://doi.org/10.1002/9780470514986.ch3>.
- Holm, N. G. & Andersson, E. M. Hydrothermal systems. in *The Molecular Origins of Life* 86–99 (Cambridge University Press, 1998). <https://doi.org/10.1017/cbo9780511626180.006>.
- Sleep, N. H., Bird, D. K. & Pope, E. C. Serpentinite and the dawn of life. *Philos. Trans. R. Soc. B Biol. Sci.* <https://doi.org/10.1098/rstb.2011.0129> (2011).
- Martin, W. & Russell, M. J. On the origin of biochemistry at an alkaline hydrothermal vent. *Philosophical Transactions of the Royal Society B: Biol. Sci.* <https://doi.org/10.1098/rstb.2006.1881> (2006).

20. Russell, M. J. The alkaline solution to the emergence of life: Energy, entropy and early evolution. *Acta Biotheor.* **55**, 133–179 (2007).
21. Martin, W., Baross, J., Kelley, D. & Russell, M. J. Hydrothermal vents and the origin of life. *Nat. Rev. Microbiol.* **6**, 805–814 (2008).
22. Martin, W. F., Sousa, F. L. & Lane, N. Energy at life's origin. *Science*. **344**, 1092–1093 (2014).
23. Russell, M. J., Hall, A. J. & Martin, W. Serpentinization as a source of energy at the origin of life. *Geobiology* **8**, 355–371 (2010).
24. Ménez, B. et al. Abiotic synthesis of amino acids in the recesses of the oceanic lithosphere. *Nature* **564**, 59–63 (2018).
25. Klein, F. et al. Iron partitioning and hydrogen generation during serpentinization of abyssal peridotites from 15°N on the Mid-Atlantic Ridge. *Geochim. Cosmochim. Acta*. **73**, 6868–6893 (2009).
26. Neuback, A. et al. Olivine alteration and H<sub>2</sub> production in carbonate-rich, low temperature aqueous environments. *Planet. Space Sci.* **96**, 51–61 (2014).
27. McCollom, T. M. Abiotic methane formation during experimental serpentinization of olivine. *Proc. Natl. Acad. Sci.* **113**, 13965–13970 (2016).
28. Templeton, A. S. Geomicrobiology of iron in extreme environments. *Elements* **7**, 95–100 (2011).
29. Suzuki, S. et al. Physiological and genomic features of highly alkaliphilic hydrogen-utilizing Betaproteobacteria from a continental serpentinizing site. *Nat. Commun.* **5**, 1–12 (2014).
30. Adam, N. & Perner, M. Microbially mediated hydrogen cycling in deep-sea hydrothermal vents. *Front. Microbiol.* **9**, 2873 (2018).
31. Ménez, B. Abiotic Hydrogen and Methane: Fuels for Life. *Elements* **16**, 39–46 (2020).
32. Berndt, M. E., Allen, D. E. & Seyfried, W. E. Reduction of CO<sub>2</sub> during serpentinization of olivine at 300°C and 500 bar. *Geology* **24**, 351–354 (1996).
33. McCollom, T. M. & Seewald, J. S. Abiotic synthesis of organic compounds in deep-sea hydrothermal environments. *Chemical Rev.* **107**, 382–401 (2007).
34. McCollom, T. M. & Seewald, J. S. Serpentinites, hydrogen, and life. *Elements* **9**, 129–134 (2013).
35. Lang, S. Q. et al. Microbial utilization of abiogenic carbon and hydrogen in a serpentinite-hosted system. *Geochim. Cosmochim. Acta*. **92**, 82–99 (2012).
36. Kohl, L. et al. Exploring the metabolic potential of microbial communities in ultra-basic, reducing springs at The Cedars, CA, USA: Experimental evidence of microbial methanogenesis and heterotrophic acetogenesis. *J. Geophys. Res. Biogeosci.* **121**, 1203–1220 (2016).
37. Cardace, D. & Hoehler, T. M. Serpentinizing Fluids Craft Microbial Habitat. *Northeast. Nat.* <https://doi.org/10.1656/045.016.0520> (2009).
38. McCollom, T. M. Geochemical constraints on sources of metabolic energy for chemolithoautotrophy in ultramafic-hosted deep-sea hydrothermal systems. *Astrobiology* **7**, 933–950 (2007).
39. Canovas, P. A., Hoehler, T. & Shock, E. L. Geochemical bioenergetics during low-temperature serpentinization: An example from the Samail ophiolite, Sultanate of Oman. *J. Geophys. Res. Biogeosci.* **122**, 1821–1847 (2017).
40. Rowe, A. R. et al. In situ electrochemical enrichment and isolation of a magnetite-reducing bacterium from a high pH serpentinizing spring. *Environ. Microbiol.* **19**, 2272–2285 (2017).
41. Meyer-Dombard, D. A. R. et al. Biofilm formation and potential for iron cycling in serpentinization-influenced groundwater of the Zambales and Coast Range ophiolites. *Extremophiles* **22**, 407–431 (2018).
42. Leong, J. A. M. & Shock, E. L. Thermodynamic constraints on the geochemistry of low-temperature, continental, serpentinization-generated fluids. *Am. J. Sci.* **320**, 185–235 (2020).
43. Nothaft, D. et al. Aqueous geochemical and microbial variation across discrete depth intervals in a peridotite aquifer assessed using a packer system in the Samail Ophiolite, Oman. *JGR Biogeosci.* <https://doi.org/10.1002/ESSOAR.10506402.2> (2021).
44. Barnes, I. & O'neil, J. R. The Relationship between Fluids in Some Fresh Alpine-Type Ultramafics and Possible Modern Serpentinization, Western United States. *GSA Bulletin* **80**, (GeoScienceWorld, 1969).
45. Neal, C. & Stanger, G. Past and present serpentinisation of ultramafic rocks; an example from the Samail ophiolite nappe of northern Oman. *Chem. Weather.* 249–275 [https://doi.org/10.1007/978-94-009-5333-8\\_15](https://doi.org/10.1007/978-94-009-5333-8_15) (1985).
46. Bruni, J. et al. Irreversible water-rock mass transfer accompanying the generation of the neutral, Mg-HCO<sub>3</sub> and high-pH, Ca-OC spring waters of the Genova province, Italy. *Appl. Geochemistry*. **17**, 455–474 (2002).
47. Hansen, L. D., Dipple, G. M., Gordon, T. M. & Kellett, D. A. Carbonated serpentinite (listwanite) at Atlin, British Columbia: A geological analogue to carbon dioxide sequestration. *Can. Mineral.* **43**, 225–239 (2005).
48. Kelemen, P. B. & Matter, J. In situ carbonation of peridotite for CO<sub>2</sub> storage. *Proc. Natl. Acad. Sci.* **105**, 17295–17300 (2008).
49. Kelemen, P. B. et al. Rates and Mechanisms of Mineral Carbonation in Peridotite: Natural Processes and Recipes for Enhanced, in situ CO<sub>2</sub> Capture and Storage. *Annu. Rev. Earth Planet. Sci.* **39**, 545–576 (2011).
50. Paukert, A. N., Matter, J. M., Kelemen, P. B., Shock, E. L. & Havig, J. R. Reaction path modeling of enhanced in situ CO<sub>2</sub> mineralization for carbon sequestration in the peridotite of the Samail Ophiolite, Sultanate of Oman. <https://doi.org/10.1016/j.chemgeo.2012.08.013> (2012).
51. Mervine, E. M., Humphris, S. E., Sims, K. W. W., Kelemen, P. B. & Jenkins, W. J. Carbonation rates of peridotite in the Samail Ophiolite, Sultanate of Oman, constrained through 14C dating and stable isotopes. *Geochim. Cosmochim. Acta* **126**, 371–397 (2014).
52. Falk, E. S. & Kelemen, P. B. Geochemistry and petrology of listwinite in the Samail ophiolite, Sultanate of Oman: Complete carbonation of peridotite during ophiolite emplacement. *Geochim. Cosmochim. Acta*. **160**, 70–90 (2015).
53. McMahon, S. et al. A Field Guide to Finding Fossils on Mars. *J. Geophysical Res. Planets*. **123**, 1012–1040 (2018).
54. Bosak, T., Moore, K. R., Gong, J. & Grotzinger, J. P. Searching for biosignatures in sedimentary rocks from early Earth and Mars. *Nat. Rev. Earth Environ.* **2**, 490–506 (2021).
55. Kelemen, P. et al. Scientific drilling and related research in the samail ophiolite, sultanate of Oman. <https://doi.org/10.15488/1062> (2013).
56. Kelemen, P. B., Matter, J. M., Teagle, D. A. H., Coggon, J. A. & Team, O. D. P. S. *Scientific Drilling in the Samail Ophiolite, Sultanate of Oman; In Proc. of the Oman Drilling Project. International Ocean Discovery Program* (2020).
57. Kelemen, P. B. et al. Initial Results From the Oman Drilling Project Multi-Borehole Observatory: Petrogenesis and Ongoing Alteration of Mantle Peridotite in the Weathering Horizon. *J. Geophys. Res. Solid Earth*. **126**, e2021JB022729 (2021).
58. Ternieten, L., Früh-Green, G. L. & Bernasconi, S. M. Carbon Geochemistry of the Active Serpentinization Site at the Wadi Tayin Massif: Insights From the ICDP Oman Drilling Project: Phase II. *J. Geophys. Res. Solid Earth*. **126**, e2021JB022712 (2021).
59. Maslov, V. P. Stromatolity. Trudy Instituta Geologicheskikh nauk. *Akad. Nauk SSSR*. **41**, 1–188 (1960).
60. Horodyski, R. J. Stromatolites of the lower Missoula Group (Middle Proterozoic), Belt Supergroup, Glacier National Park, Montana. *Precambrian Res.* [https://doi.org/10.1016/0301-9268\(75\)90010-8](https://doi.org/10.1016/0301-9268(75)90010-8) (1975).
61. Walter, M. R. & Awramik, S. M. Frutexites from stromatolites of the Gunflint Iron Formation of Canada, and its biological affinities. *Precambrian Res.* **9**, 23–33 (1979).
62. Bengtson, S. et al. Deep-biosphere consortium of fungi and prokaryotes in Eocene seafloor basalts. *Geobiology* **12**, 489–496 (2014).
63. Guido, A., Rosso, A., Sanfilippo, R., Russo, F. & Mastandrea, A. Frutexites from microbial/metazoan bioconstructions of recent and Pleistocene marine caves (Sicily, Italy). *Palaeogeogr. Palaeoclimatol. Palaeoecol.* **453**, 127–138 (2016).
64. Heim, C., Quéric, N. V., Ionescu, D., Schäfer, N. & Reitner, J. Frutexites-like structures formed by iron oxidizing biofilms in the continental subsurface (Åspö Hard Rock Laboratory, Sweden). *PLoS One*. **12**, e0177542 (2017).
65. Jakubowicz, M., Belka, Z. & Berkowski, B. Frutexites encrustations on rugose corals (Middle Devonian, southern Morocco): Complex growth of microbial microstromatolites. *Facies* <https://doi.org/10.1007/s10347-013-0381-1> (2014).
66. Kudryavtsev, A. B., Schopf, J. W., Agresti, D. G. & Wdowiak, T. J. In situ laser-Raman imagery of precambrian microscopic fossils. *Proc. Natl. Acad. Sci.* **98**, 823–826 (2001).
67. Schopf, J. W., Kudryavtsev, A. B., Agresti, D. G., Wdowiak, T. J. & Czaja, A. D. Laser-Raman imagery of Earth's earliest fossils. *Nature* **416**, 73–76 (2002).
68. Sherman, D. M. & Waite, T. D. Electronic spectra of Fe<sup>3+</sup> oxides and oxide hydroxides in the near IR to near UV. *Am. Mineral.* **70**, 1262–1269 (1985).
69. Scheinost, A. C., Chavernas, A., Barrón, V. & Torrent, J. Use and limitations of second-derivative diffuse reflectance spectroscopy in the visible to near-infrared range to identify and quantify Fe oxide minerals in soils. *Clays Clay Miner.* **46**, 528–536 (1998).
70. Burns, R. G. Rates and mechanisms of chemical weathering of ferromagnesian silicate minerals on Mars. *Geochim. Cosmochim. Acta*. **57**, 4555–4574 (1993).
71. Cloutis, E. A., Hiroi, T., Gaffey, M. J., Alexander, C. M. O. D. & Mann, P. Spectral reflectance properties of carbonaceous chondrites: 1. CI chondrites. *Icarus* **212**, 180–209 (2011).
72. McCollom, T. M. et al. Hydrogen generation and iron partitioning during experimental serpentinization of an olivine-pyroxene mixture. *Geochim. Cosmochim. Acta*. **282**, 55–75 (2020).
73. Buick, R. Microfossil recognition in Archean rocks: an appraisal of spheroids and filaments from a 3500 m.y. old chert-barite unit at North Pole, Western Australia. *Palaios* **5**, 441–459 (1990).
74. William Schopf, J., Kudryavtsev, A. B., Sugitani, K. & Walter, M. R. Precambrian microbe-like pseudofossils: A promising solution to the problem. *Precambrian Res.* <https://doi.org/10.1016/j.precamres.2010.03.003> (2010).
75. Brasier, M. D. & Wacey, D. Fossils and astrobiology: New protocols for cell evolution in deep time. *Int. J. Astrobiol.* <https://doi.org/10.1017/S147350412000298> (2012).
76. Brasier, M. D. et al. Questioning the evidence for Earth's oldest fossils. *Nature* **416**, 76–81 (2002).

77. García-Ruiz, J. M. et al. Self-Assembled Silica-Carbonate Structures and Detection of Ancient Microfossils. *Science*. **302**, 1194–1197 (2003).
78. Cosmidis, J. & Templeton, A. S. Self-assembly of biomorphic carbon/sulfur microstructures in sulfidic environments. *Nat. Commun.* **7**, 12812 (2016).
79. Cosmidis, J., Nims, C. W., Diercks, D. & Templeton, A. S. Formation and stabilization of elemental sulfur through organomineralization. *Geochim. Cosmochim. Acta*. **247**, 59–82 (2019).
80. McMahon, S. Earth's earliest and deepest purported fossils may be iron-mineralized chemical gardens. *Proc. R. Soc. B Biol. Sci.* **286**, 20192410 (2019).
81. Nims, C., Lafond, J., Alleon, J., Templeton, A. S. & Cosmidis, J. Organic biomorphs may be better preserved than microorganisms in early Earth sediments. *Geology* **49**, e1602285 (2021).
82. García-Ruiz, J. M., Nakouzi, E., Kotopoulou, E., Tamborrino, L. & Steinbock, O. Biomimetic mineral self-organization from silica-rich spring waters. *Sci. Adv.* **3**, 160–170 (2017).
83. McMahon, S. et al. Dubiofossils from a Mars-analogue subsurface palaeoenvironment: The limits of biogenicity criteria. *Geobiology* **19**, 473–488 (2021).
84. Rouillard, J., García-Ruiz, J.-M., Gong, J. & Van Zuilen, M. A. A morphogram for silica-witherite biomorphs and its application to microfossil identification in the early earth rock record. *Geobiology* **16**, 279–296 (2018).
85. Krepeski, S. T., Emerson, D., Hredzak-Showalter, P. L., Luther, G. W. & Chan, C. S. Morphology of biogenic iron oxides records microbial physiology and environmental conditions: Toward interpreting iron microfossils. *Geobiology* **11**, 457–471 (2013).
86. Ivarsson, M. et al. Fossilized fungi in subseafloor Eocene basalts. *Geology* **40**, 163–166 (2012).
87. Schopf, J. W., Kudryavtsev, A. B., Czaja, A. D. & Tripathi, A. B. Evidence of Archean life: Stromatolites and microfossils. *Precambrian Res.* **158**, 141–155 (2007).
88. Oehler, D. Z. et al. NanoSIMS: Insights to biogenicity and syngeneity of Archean carbonaceous structures. *Precambrian Res.* **173**, 70–78 (2009).
89. Stüeken, E. E., Zaloumis, J., Meixnerová, J. & Buick, R. Differential metamorphic effects on nitrogen isotopes in kerogen extracts and bulk rocks. *Geochim. Cosmochim. Acta*. **217**, 80–94 (2017).
90. Kilburn, M. R. & Wacey, D. NanoSIMS analysis of Archean fossils and biomarkers. *Appl. Surf. Sci.* **255**, 1465–1467 (2008).
91. Hallberg, R. & Ferris, F. G. Biomineralization by *Gallionella*. *Geomicrobiol. J.* **21**, 325–330 (2004).
92. Szulczewski, M. Stromatolites from the high-arctic Bathonian of the Tatra Mountains. *Acta Geol. Pol.* **13**, 125–141 (1963).
93. Hofmann, H. J. Stromatolites from the Proterozoic Animikie and Sibley Groups, Ontario. *Dep. Energy, Mines Resour.* **68**, 1–77 (1969).
94. Böhm, F. & Brachert, T. C. Deep-water stromatolites and Frutexitex Maslov from the early and Middle Jurassic of S-Germany and Austria. *Facies* **28**, 145–168 (1993).
95. Cavalazzi, B., Barbieri, R. & Ori, G. G. Chemosynthetic microbialites in the Devonian carbonate mounds of Hamar Laghdad (Anti-Atlas, Morocco). *Sediment. Geol.* **73–88** <https://doi.org/10.1016/j.sedgeo.2007.03.002> (2007).
96. Lollar, B. S. et al. Hydrogeologic controls on episodic H<sub>2</sub> release from Precambrian fractured rocks - energy for deep subsurface life on Earth and Mars. *Astrobiology* **7**, 971–986 (2007).
97. Leong, J. A. M. et al. Theoretical Predictions vs Environmental Observations on Serpentinization Fluids: Lessons from the Samail Ophiolite in Oman. *J. Geophys. Res. Solid Earth*. **126**, e2020JB020756 (2021).
98. Nothhaft, D. B. et al. Geochemical, Biological, and Clumped Isotopologue Evidence for Substantial Microbial Methane Production Under Carbon Limitation in Serpentinites of the Samail Ophiolite, Oman. *J. Geophys. Res. Biogeosci.* **126**, e2020JG006025 (2021).
99. Miller, H. M. et al. Modern water/rock reactions in Oman hyperalkaline peridotite aquifers and implications for microbial habitability. *Geochim. Cosmochim. Acta*. **179**, 217–241 (2016).
100. Iyer, K., Jamtveit, B., Mathiesen, J., Malthe-Sørenssen, A. & Feder, J. Reaction-activated hierarchical fracturing during serpentinization. *Earth Planet. Sci. Lett.* **267**, 503–516 (2008).
101. Kelemen, P. B. & Hirth, G. Reaction-driven cracking during retrograde metamorphism: Olivine hydration and carbonation. *Earth Planet. Sci. Lett.* **345–348**, 81–89 (2012).
102. Evans, O., Spiegelman, M. & Kelemen, P. B. A Poroelastic Model of Serpentinization: Exploring the Interplay Between Rheology, Surface Energy, Reaction, and Fluid Flow. *J. Geophys. Res. Solid Earth*. **123**, 8653–8675 (2018).
103. Evans, O., Spiegelman, M. & Kelemen, P. B. Phase-Field Modeling of Reaction-Driven Cracking: Determining Conditions for Extensive Olivine Serpentinization. *J. Geophys. Res. Solid Earth*. **125**, e2019JB018614 (2020).
104. Lafay, R., Montes-Hernandez, G., Renard, F. & Vonlanthen, P. Intracrystalline Reaction-Induced Cracking in Olivine Evidenced by Hydration and Carbonation Experiments. *Minerals* **8**, 412 (2018).
105. Peuble, S. et al. Multi-scale characterization of the incipient carbonation of peridotite. *Chem. Geol.* **476**, 150–160 (2018).
106. Zheng, X., Cordonnier, B., Zhu, W., Renard, F. & Jamtveit, B. Effects of Confinement on Reaction-Induced Fracturing During Hydration of Periclase. *Geochemistry, Geophys. Geosystems*. **19**, 2661–2672 (2018).
107. Kelemen, P. B. et al. Correlated variation in vein type, vein frequency, pH, oxygen fugacity and depth in Oman Drilling Project Holes BA1B, BA3A and BA4A. **2018**, (2018).
108. Klein, F. et al. Fluid mixing and the deep biosphere of a fossil Lost City-type hydrothermal system at the Iberia Margin. *Proc. Natl. Acad. Sci.* **112**, 12036–12041 (2015).
109. Zwicker, J. et al. Evidence for archaeal methanogenesis within veins at the onshore serpentinite-hosted Chimaera seeps, Turkey. *Chem. Geol.* **483**, 567–580 (2018).
110. Newman, S. A. et al. Lipid Biomarker Record of the Serpentinite-Hosted Ecosystem of the Samail Ophiolite, Oman and Implications for the Search for Biosignatures on Mars. *Astrobiology* **20**, 830–845 (2020).
111. Ménez, B., Pasini, V. & Brunelli, D. Life in the hydrated suboceanic mantle. *Nat. Geosci.* **5**, 133–137 (2012).

## Acknowledgements

We gratefully acknowledge the Oman Drilling Science Party for facilitating access and characterization of these materials. We would like to thank Timothy Hahn for assistance during NanoSIMS analysis at the ASU Center for Isotope Analysis, and Jakob Thyr for assistance during Raman analysis at the Ångström Laboratory. We also thank Bethany Ehlmann for use of her imaging spectrometer and thank her and Elena Amador for assistance with those measurements. This material is based upon work supported by the National Science Foundation Graduate Research Fellowship under Grant No. 1841051, and by the NSF GROW program. MB would like to thank the NSF EAR grant 1819550 (PI: Richard Hervig). This research used logistical support, samples and data provided by the Oman Drilling Project. The Oman Drilling Project has been possible through co-mingled funds from the International Continental Scientific Drilling Project (ICDP, lead PI's Kelemen, Matter & Teagle), the Sloan Foundation – Deep Carbon Observatory (Grant 2014-3-01, Kelemen PI), the National Science Foundation (NSF-EAR-1516300, Kelemen PI), the NASA Astrobiology Institute (NNA15BB02A, Templeton PI), the German Research Foundation (DFG, Koepke PI), the Japanese Society for the Promotion of Science (JSPS, 16H06347, Michibayashi PI, and 19H00730, Morono PI), the European Research Council (Jamtveit PI), the Swiss National Science Foundation (Früh-Green PI), the Japanese Marine Science and Technology Center (JAMSTEC), the TAMU-JR Science operator, and in-kind contributions from the Sultanate of Oman Ministry of Regional Municipalities and Water Resources, the Oman Public Authority of Mining, Sultan Qaboos University, CRNS- Univ. Montpellier II, Columbia University, and the University of Southampton.

## Author contributions

J.L.Z. conceptualized the project, selected samples during Oman DP Phase 2 shipboard activity, and conducted microscopy, Raman spectroscopy, SEM/EDS, and NanoSIMS. A.N. and M.I. assisted in conceptualizing the project, assisted during instrumental analyses, and provided extensive interpretation of data. M.B. assisted with NanoSIMS analyses and interpretation. R.G. provided VSWIR data and interpretations on mineral phase identification and distribution. A.S.T. provided field geochemical data of the active Samail Ophiolite as well as interpretations on biogenicity and the habitability of the selected samples. A.D.C. and T.E. provided Raman spectral data and interpretations on biogenicity. P.K. provided interpretations on vein formation, geologic context, and age data.

## Competing interests

The authors declare no competing interests.

## Additional information

**Supplementary information** The online version contains supplementary material available at <https://doi.org/10.1038/s43247-022-00551-1>.

**Correspondence** and requests for materials should be addressed to Jon Lima-Zaloumis.

**Peer review information** *Communications Earth & Environment* thanks the anonymous reviewers for their contribution to the peer review of this work. Primary Handling Editors: Clare Davis. Peer reviewer reports are available.

**Reprints and permission information** is available at <http://www.nature.com/reprints>

**Publisher's note** Springer Nature remains neutral with regard to jurisdictional claims in published maps and institutional affiliations.



**Open Access** This article is licensed under a Creative Commons Attribution 4.0 International License, which permits use, sharing, adaptation, distribution and reproduction in any medium or format, as long as you give appropriate credit to the original author(s) and the source, provide a link to the Creative Commons license, and indicate if changes were made. The images or other third party material in this article are included in the article's Creative Commons license, unless indicated otherwise in a credit line to the material. If material is not included in the article's Creative Commons license and your intended use is not permitted by statutory regulation or exceeds the permitted use, you will need to obtain permission directly from the copyright holder. To view a copy of this license, visit <http://creativecommons.org/licenses/by/4.0/>.

© The Author(s) 2022